PHYSICAL REVIEW APPLIED **14,** 034066 (2020)

Superresolution Imaging via Subwavelength Hole Resonances

Junshan Lin[1,*] and Hai Zhang[2,†]

[1] *Department of Mathematics and Statistics, Auburn University, Auburn, Alabama 36849, USA*
[2] *Department of Mathematics, HKUST, Clear Water Bay, Kowloon, Hong Kong S.A.R., China*

(Received 2 June 2020; revised 29 July 2020; accepted 25 August 2020; published 28 September 2020)

This work presents a superresolution imaging approach by using subwavelength hole resonances. We employ a subwavelength structure in which an array of tiny holes are etched in a metallic slab with the neighboring distance ℓ that is smaller than half of the wavelength. By tuning the frequencies of the incident wave at resonant frequencies, the subwavelength structure generates strong illumination patterns that are able to probe both low and high spatial frequency components of the imaging sample sitting above the structure. The image of the sample is obtained by performing stable numerical reconstruction from the far-field measurement of the diffracted wave. It is demonstrated that a resolution of $\ell/2$ can be obtained for reconstructed images, thus one can achieve superresolution by arranging multiple holes within one wavelength. The proposed approach may find applications in microscopies as well as wave-based imaging such as electromagnetic and ultrasound imaging. It attains two advantages that are important for practical realization. It avoids the difficulty of controlling the distance between the probe and the sample surface with high precision. In addition, the numerical reconstructed images are very stable against noise by only using the low-frequency band of the far-field data in the numerical reconstruction.

DOI: 10.1103/PhysRevApplied.14.034066

I. INTRODUCTION

Due to the wave nature of the optical light, the resolution of conventional microscopies is typically constrained by the Rayleigh criterion (or *Abbe's diffraction limit*) [1–3]. Enormous efforts have been devoted to achieve images beyond the diffraction limit in the last several decades. One main class of microscopies achieve superresolution by *near-field* technologies, where one probes the samples or collects the diffracted optical field in the vicinity of the object (typically within one wavelength) [4–7]. The principle of high resolution is provided by taking into account of evanescent waves, which decay exponentially at the object's surface. The main limitation of such microscopies, however, lies in the need to control the distance of the probe over the sample surface with extremely high precision and very shallow penetration depth of optical field. Therefore, there has been intensive efforts to explore superresolution techniques without relying on near-field illumination and measurement. Among those there are two main successful approaches. One is the fluorescence type, which relies on emission from fluorescent molecules and photon switching to localize a single molecular [8–10]. The other is to use structured illumination to provide high-spatial-frequency wave pattern so as to shrink the support of point-spread function [11–13]. However, so far microscopies based on structured illumination can only improve Abbe's diffraction limit by a factor of 2 [11].

Mathematically, the inverse scattering theory can be applied to understand how the structure of a scattering object is encoded in measured wave fields in the near-field scanning optical microscopy and other related imaging problems [14–20]. Numerical approaches have also been explored extensively to achieve superresolution imaging of point sources and other related problems when only far-field data is collected (cf. Refs. [21–24] and references therein).

A. Roadmap for superresolution imaging

Motivated by our recent work on the quantitative analysis of the resonances for various subwavelength hole structures [25–32], in this paper we propose a superresolution imaging modality with illumination patterns generated by a collection of coupled subwavelength holes. The original work of subwavelength hole array and the induced extraordinary optical transmission (EOT) dates back to about two decades ago [33], and this type of nanostructure has found important applications in biological and chemical sensing, and other optical devices; see, for instance, [34–37].

The new illumination patterns are the resonant modes of the hole structures, which oscillate on a subwavelength

---

[*] jzl0097@auburn.edu
[†] haizhang@ust.hk

scale. They can probe both the low- and high-spatial-frequency components of the sample, and very importantly, transfer such information to the lower-frequency band of the wave field after its interaction with the sample and then propagate to the far-field detector plane. As such the high-spatial-frequency components of the sample can be recovered through numerical inversion of the data measured in the far field and one can achieve the superresolution image for the sample. We point out that subwavelenghth resonant modes using Helmholtz resonators can also give rise to the superfocusing and superresolution [38,39].

Let us describe the main idea for the above roadmap in the ideal case over the x_1-x_2 plane. Suppose one would like to image a one-dimensional sample characterized by its transmission function $q(x_1)$ and the sample sits on the x_1 axis. Let λ be the free-space wavelength of the optical wave, and $k = 2\pi/\lambda$ be the corresponding wave number. Consider illuminating the sample from below with a pattern given by $u_m = e^{imkx_1 - \zeta x_2}$ for an integer m, in which $(mk)^2 - \zeta^2 = k^2$ such that u_m satisfies the frequency–domain-wave equation with the wave number k. Then under the assumption that the interaction between the illumination and the sample is negligible, the field through the sample becomes $v_m(x_1, 0) := u_m(x_1, 0)q(x_1)$, which then propagates to the detector plane $x_2 = d \gg \lambda$. In the Fourier domain, this can be expressed as $\hat{v}_m(\xi, d) = e^{i\rho_0(\xi)d}\hat{v}_m(\xi, 0)$, in which

$$\rho_0(\xi) = \begin{cases} \sqrt{k^2 - \xi^2}, & |\xi| \le k, \\ i\sqrt{\xi^2 - k^2}, & |\xi| > k. \end{cases}$$

Note that only the propagating modes of the transmitted field, or $\hat{v}_m(\xi, 0)$ with low spatial frequencies $\xi \in \Omega_k := [-k, k]$, can reach the far-field detector plane and be collected. Hence in the ideal scenario when the full-aperture data is available, $\hat{v}_m(\xi, 0)$ for $\xi \in \Omega_k$ can be recovered from the far-field measurement in the Fourier domain. From the formula

$$\hat{v}_m(\xi, 0) = \hat{u}_m(\xi, 0) * \hat{q}(\xi) = \hat{q}(\xi - mk) \quad \text{for } \xi \in \Omega_k, \tag{1}$$

one deduces that the Fourier components $\hat{q}(\xi)$ for $\xi \in \Omega_k - mk$ is recovered from the far-field data (see Fig. 1). Therefore, by varying m from $-M$ to M, one recovers all the Fourier components of the sample transmission q in the frequency band $[-(M+1)k, (M+1)k]$ and the superresolution can be achieved if $M > 1$.

In this paper we employ the subwavelength holes to generate wave patterns that mimic the desired oscillations of the ideal illuminations $u_m = e^{imkx_1 - \zeta x_2}$. These can be realized by arranging the subwavelength holes in an array and tuning the incidence frequencies at corresponding resonant frequencies as discussed in what follows.

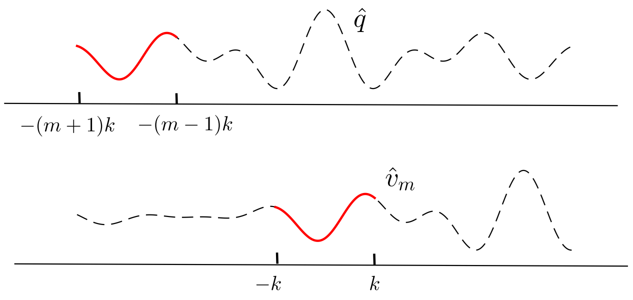

FIG. 1. Shift of $\hat{q}_m(\xi - mk)$ to $\hat{v}_m(\xi, 0)$ for $\xi \in \Omega_k$ when interacting with the illumination pattern u_m.

B. Proposed imaging setup and an overview of the imaging approach

We focus on the imaging problem in the two-dimensional configuration, in which the subwavelength structure consists of an array of identical slit holes $S_1, S_2, \ldots, S_J$ patterned in a metallic slab. The slits are invariant along the x_3 direction and Fig. 2 shows a schematic plot of the imaging setup on the x_1-x_2 plane. The slits are arranged in a manner such that $\ell < \lambda/2$ and $J\ell = O(\lambda)$, where ℓ denotes the distance between the adjacent slits, or more precisely, the distance between the left walls of two adjacent slit holes (see Fig. 2). In addition, each slit hole has a width of δ and there holds $\delta \ll \ell$. The tiny slit holes can be etched by sculpting techniques such as focused ion-beam lithography or atomic layer lithography [40,41]. The imaging sample is deposited over a thin substrate (e.g., glass) sitting on top of the metallic slab with a thickness $h \ll \lambda$. When an incident wave impinges from below the slab, it transmits through the slit holes and generates a wave pattern that interacts with the sample in the near field. The corresponding diffracted field is then collected on the far-field detector plane.

Remark 1. *The substrate is introduced here for the purpose of practical realization of the imaging setup. It controls the near-field interaction between the slit holes and*

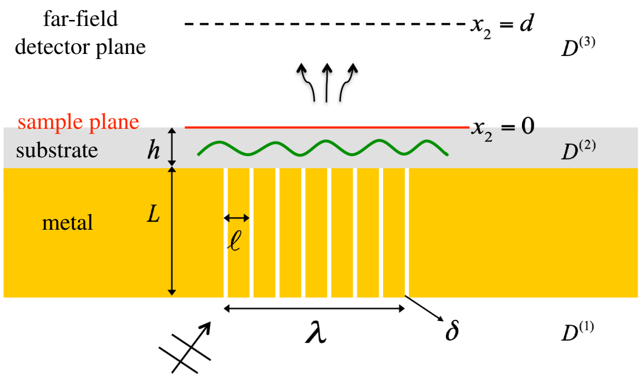

FIG. 2. Schematic plot of the imaging setup on the x_1-x_2 plane.

the sample. Smaller h allows more interactions, which may result in higher resolution in the reconstructed image. It should be noted that resonant frequencies of the slit holes is more sensitive to the change of the substrate thickness when $h < \delta$ [31]. We also emphasize that the inclusion of the substrate does not induce an essential difference for the mathematical modeling of the imaging problem and its numerical reconstruction.

For clarity of exposition, throughout the paper we formulate the problem in a dimensionless coordinate system by assuming that the slab and the substrate attains a thickness of $L = 1$ and $L = O(\lambda)$. We also adopt the coordinate system on the x_1-x_2 plane such that the origin is located on the sample plane. The support of the imaging sample on the sample plane is denoted by $I_0 = [0, a]$. Let a_1 and a_J be the x_1 coordinate of the left wall of S_1 and the right wall of S_J, respectively. It is assumed that $I_0 \subset I_{\text{slit}} := [a_1, a_J]$ such that the support of the imaging sample is covered by the region that the slit apertures span. For simplicity we assume that $a_1 = 0$.

The subwavelength structure attains a series of complex-valued resonances lying below the real axis. At the resonant frequencies (the real part of complex-valued resonances), the transmission through the slit holes exhibit peak values and the transmitted wave field is strong. In the periodic case, almost total transmission can be achieved at the resonant frequencies [27,28]. By tuning the frequency of the incidence field at several resonant frequencies only, the transmitted wave patterns sweep from low to high frequencies, which allows for probing both the low- and high-spatial-frequency components of the sample. The resonances and wave patterns at resonant frequencies are investigated in detail in Sec. II.

To obtain the sample image in a realistic configuration where only limited-aperture data is available, one can not perform the reconstruction in the Fourier domain directly. Instead, we formulate and solve the underlying inverse problem in the spatial domain and present numerical algorithms to perform the reconstruction. This is elaborated in Sec. III where two approaches, one based on the gradient-descent method and the other on the total variation regularization with the split Bregman iteration, are presented. One important feature of our numerical reconstruction for the underlying imaging problem is that they are stable against noise, since only the lower-frequency band Ω_k of the measured data is used, while the noise is typically highly oscillatory. This is illustrated in Secs. III and IV when the numerical algorithms and the numerical examples are presented.

In view of relation (1), the resolution of the image depends on the oscillation patterns of the illumination, which is further determined by the distance ℓ between two adjacent slit holes in the proposed imaging setup. From various numerical examples given in Sec. III and IV, we observe that the image resolution is about $\ell/2$. Therefore, a high-resolution image can be obtained by arranging multiple holes within one wavelength.

II. RESONANT SCATTERING BY A COLLECTION OF SUBWAVELENGTH HOLES

We formulate the mathematical model in the context of transverse-magnetic electromagnetic wave scattering. The same model holds for acoustic waves, where one replaces the optical refractive index by the acoustic refractive index. The domain below the metallic slab, the substrate domain and the domain above the substrate is denoted by $D^{(1)}$, $D^{(2)}$, and $D^{(3)}$, respectively. For each slit hole S_j, let $\Gamma_j^{(1)}$ and $\Gamma_j^{(2)}$ denote the lower and upper slit apertures, respectively. Let $D_\delta := \cup_{j=1}^{J} S_j$ be the slit region, and $\Gamma^{(1)}$ and $\Gamma^{(2)}$ be the union of the lower and upper slit apertures $\Gamma_j^{(1)}$ and $\Gamma_j^{(2)}$, respectively. Then the relative permittivity ε is given by

$$\varepsilon(x) = \begin{cases} \varepsilon_0 = 1 & \text{for } x \in D^{(1)} \cup D^{(3)} \cup D_\delta, \\ \varepsilon_h > 1 & \text{for } x \in D^{(2)}, \end{cases}$$

and the refractive index is $n(x) = \sqrt{\varepsilon(x)}$.

For the transverse-magnetic polarization with the magnetic field $H = (0, 0, u)$, Maxwell's equations reduce to the scalar Helmholtz equation in two dimensions. Let $u_{\text{inc}} = e^{ik(x_1 \sin\theta + x_2 \cos\theta)}$ be the incident plane wave that impinges from below the slab. Denote the exterior region of the metal by D. Then the total field u satisfies

$$\begin{aligned} &\nabla \cdot \left[\frac{1}{\varepsilon(x)} \nabla u\right] + k^2 u = 0 \quad \text{in } D, \\ &\frac{\partial u}{\partial \nu} = 0 \quad \text{on } \partial D, \\ &[u] = 0, \quad \left[\frac{1}{\varepsilon}\frac{\partial u}{\partial \nu}\right] = 0 \quad \text{on } \partial D^{(3)} \cup \Gamma^{(2)}. \end{aligned} \tag{2}$$

In the above, $[\cdot]$ denotes the jump of the quantity when the limit is taken along the positive and negative unit normal direction ν. In addition, the diffracted field $u_{\text{diff}} := u - u^{\text{inc}}$ satisfies outgoing radiation conditions at infinity.

It can be shown that the scattering problem (2) attains a unique solution for all complex wave number k with $\Im k \geq 0$. Moreover, the resolvent for the corresponding differential operator attains a countable number of poles when continued meromorphically to the whole complex plane. These poles are called the resonances (or scattering resonances) of the scattering problem, and the associated resonant states (quasinormal modes) decay in time but grow exponentially away from the slab.

To obtain the resonances, we consider the problem (2) when the incident wave $u_{\text{inc}} = 0$ and set up an integral equation formulation [42]. Let $g^{(1)}(x,y)$ be Green's function in the domain $D^{(1)}$ with the Neumann boundary condition along the metallic slab boundary. Applying Green's formula in $D^{(1)}$ gives

$$u(x) = -\sum_{j=1}^{J} \int_{\Gamma_j^{(1)}} g^{(1)}(x,y)\, \partial_2 u(y_-) ds_y, \quad x \in D^{(1)}.$$

Here and henceforth, $\partial_2 u(y_\pm)$ denotes the limit of the given function $\partial u(x)/\partial x_2$ when x approaches the aperture from the above and below, respectively. Similarly, using the layered Green function $g^{(2)}(x,y)$ in the domain $D^{(2)} \cup D^{(3)}$ with the Neumann boundary condition along the metallic slab boundary, one obtains

$$u(x) = \sum_{j=1}^{J} \int_{\Gamma_j^{(2)}} g^{(2)}(x,y)\, \partial_2 u(y_+) ds_y, \quad x \in D^{(2)}.$$

The derivation of Green's function in layered medium is given in the Appendix. Let

$$g_j(x,y) := g_0[x_1 - (j-1)\ell, x_2; y_1 - (j-1)\ell, y_2]$$

be Green's function inside the slit S_j with the Neumann boundary condition along the boundary of S_j, in which

$$g_0(k;x,y) = \sum_{m,n=0}^{\infty} c_{mn}\phi_{mn}(x)\phi_{mn}(y),$$

with $c_{mn} = [k^2 - (m\pi/\delta)^2 - (n\pi)^2]^{-1}$, $\phi_{mn}(x) = \sqrt{\beta_{mn}/\delta} \cos[(m\pi/\delta)x_1]\cos(n\pi x_2)$, and

$$\beta_{mn} = \begin{cases} 1 & m = n = 0, \\ 2 & m = 0, n \geq 1 \quad \text{or} \quad n = 0, m \geq 1, \\ 4 & m \geq 1, n \geq 1. \end{cases}$$

Then the solution inside the slit S_j can be expressed as

$$u(x) = \int_{\Gamma_j^{(1)}} g_j(x,y)\, \partial_2 u(y_+) ds_y - \int_{\Gamma_j^{(2)}} g_j(x,y) \partial_2 u(y_-) ds_y$$

for $x \in S_j$.

By taking the limit of the above integral to the slit apertures and imposing the continuity condition of the electromagnetic field over the slit apertures, we obtain the following system of boundary integral equations for $j = 1, 2, \ldots, J$:

$$\begin{aligned} &\sum_{j=1}^{J} \int_{\Gamma_j^{(1)}} g^{(1)}(x,y)\varphi_j^{(1)}(y) ds_y + \int_{\Gamma_j^{(1)}} g_j(x,y)\varphi_j^{(1)}(y) ds_y \\ &\quad + \int_{\Gamma_j^{(2)}} g_j(x,y)\varphi_j^{(2)}(y) ds_y = 0 \quad \text{on } \Gamma_j^{(1)}, \\ &\varepsilon_h \sum_{j=1}^{J} \int_{\Gamma_j^{(2)}} g^{(2)}(x,y)\varphi_j^{(2)}(y) ds_y + \int_{\Gamma_j^{(1)}} g_j(x,y)\varphi_j^{(1)}(y) ds_y \\ &\quad + \int_{\Gamma_j^{(2)}} g_j(x,y)\varphi_j^{(2)}(y) ds_y = 0 \quad \text{on } \Gamma_j^{(2)}, \end{aligned} \tag{3}$$

where $\varphi_j^{(1)} := -\partial_2 u(y_+)|_{\Gamma_j^{(1)}} = -\partial_2 u(y_-)|_{\Gamma_j^{(1)}}$ and $\varphi_j^{(2)} := \partial_2 u(y_-)|_{\Gamma_j^{(2)}} = (1/\varepsilon_h)\partial_2 u(y_+)|_{\Gamma_j^{(2)}}$.

The resonances are the characteristic values k of the above integral equations for which nontrivial solutions $\{\varphi_j^{(1)}, \varphi_j^{(2)}\}_{j=1}^{J}$ exist. When $J = 1$, the analytical expression for the resonances can be obtained through the asymptotic analysis of the integral equation and the Gohberg-Sigal theory. It can be shown that (cf. Ref. [31]) the resonances obtain the following asymptotic expansion for integer m satisfying $m\delta \ll 1$:

$$\begin{aligned} k^{(m)} &= m\pi + m(\varepsilon_h + 1)\delta \ln\delta + 2m\pi c_{m,H}\delta \\ &\quad + O(\delta^2 \ln^2 \delta), \end{aligned}$$

where the complex-valued constant $c_{m,H} = O(1)$ is independent of δ. Namely, the real part of the resonances is close to $m\pi$ and their imaginary parts are of order $O(\delta)$.

When $J > 1$, the coupling of the subwavelength holes will generate a group of resonances $\{k_{m1}, \ldots, k_{mJ}\}$ for each m satisfying $m\delta \ll 1$. The existence of resonances in this scenario can still be proved rigorously by applying the asymptotic expansion for Eq. (3) and the Gohberg-Sigal theory. This boils down to solving for the roots of nonlinear functions $\gamma_1(k), \ldots, \gamma_J(k)$, where each attains a simple root near $m\pi$ for each given integer m. We refer the reader to Ref. [25] for such a rigorous analysis when $J = 2$. Here we obtain the resonances by solving Eq. (3) numerically. The computational approach we adopt follows the lines in Ref. [29], where a high-order numerical discretization of the integral operators as well as their fast implementation is achieved by a combination of the Nystrom scheme for singular kernels, a contour integration approach for the layered Green function $g^{(2)}(x,y)$, and a Kummer transformation acceleration strategy for evaluation of the series in Green's function $g_j(x,y)$. For a subwavelength structure with $\ell = 0.2$ and $\delta = 0.02$, the resonances with $J = 3$ and $J = 6$ are collected in Tables I and II, respectively, for $m = 1, 2, 3$. Here we set the substrate thickness as $h = 0.1$, and its relative permittivity as $\varepsilon_h = 2$.

TABLE I. Resonances with $J = 3$, $\ell = 0.2$, and $\delta = 0.02$.

	$k_{1,j}$	$k_{2,j}$	$k_{3,j}$
$j = 1$	$2.8620 - 0.1791i$	$5.7941 - 0.1412i$	$8.7233 - 0.0949i$
$j = 2$	$2.8977 - 0.0193i$	$5.8625 - 0.0131i$	$8.8395 - 0.3822i$
$j = 3$	$2.9454 - 0.0013i$	$5.9447 - 0.2737i$	$9.0325 - 0.2863i$

Note that at the resonant frequency $k = \Re\, k_{mj}$, the transmitted field u_{tran} is amplified by an order that is inversely proportional to $\Im\, k_{mj}$. On the other hand, due to the smallness of δ, u_{tran} can be viewed as the field generated by an array of point charges α_j located at the hole aperture $\Gamma_j^{(2)}$ [26,28]. Depending on the resonance frequencies, α_j can be positive or negative, which induces different oscillatory patterns for u_{tran}. This is illustrated in Figs. 3 and 4 for $J = 6$, where the transmitted field u_{tran} on the sample plane $x_2 = 0$ and in the region $[-4, 5] \times [0, 1]$ above the sample plane is shown at the resonant frequencies $k = \Re\, k_{1j}$ for $j = 1, 2, \ldots, 6$, respectively.

III. SUPERRESOLUTION IMAGING OF INFINITELY THIN SAMPLES

A. Formulation of the imaging problem

We first consider the configuration where the sample is an infinitely thin sheet. The thin sheet can be produced, for instance, by microcontact printing [43]. This allows us to ignore the topography-induced effect and the multiple scattering between the illumination and the sample [2].

Let u_{tran} be the transmitted field through the subwavelength holes. Assume that the thin sheet, which is deposited on the sample plane $x_2 = 0$, is characterized by the transmission function $q(x_1)$ with $0 \le q(x_1) \le 1$. Then the wave field after being transmitted immediately through the sample is given by $u_{\text{samp}}(x_1, 0) = q(x_1) u_{\text{tran}}(x_1, 0)$. The propagation of the sample field u_{samp} to the detection plane $x_2 = d$ is described by the propagator (transfer function) in the Fourier domain:

$$\hat{u}_{\text{det}}(\xi, d) = e^{i\rho_0(\xi) d}\, \hat{u}_{\text{samp}}(\xi, 0), \tag{4}$$

where

$$\rho_0(\xi) = \begin{cases} \sqrt{k^2\varepsilon_0 - \xi^2}, & |\xi| \le k, \\ i\sqrt{\xi^2 - k^2\varepsilon_0}, & |\xi| > k. \end{cases}$$

TABLE II. Resonances with $J = 6$, $\ell = 0.2$, and $\delta = 0.02$.

	$k_{1,j}$	$k_{2,j}$	$k_{3,j}$
$j = 1$	$2.8080 - 0.1186i$	$5.6934 - 0.2542i$	$8.6576 - 0.1087i$;
$j = 2$	$2.8826 - 0.0146i$	$5.7850 - 0.0472i$	$8.6678 - 0.4521i$
$j = 3$	$2.9213 - 0.2423i$	$5.8559 - 0.0087i$	$8.7540 - 0.0135i$
$j = 4$	$2.9248 - 0.0032i$	$5.8862 - 0.0014i$	$9.0356 - 0.3623i$
$j = 5$	$2.9439 - 0.0008i$	$5.9533 - 0.3190i$	$9.0368 - 0.2838i$
$j = 6$	$2.9529 - 0.0002i$	$6.0067 - 0.2431i$	$9.0381 - 0.2680i$

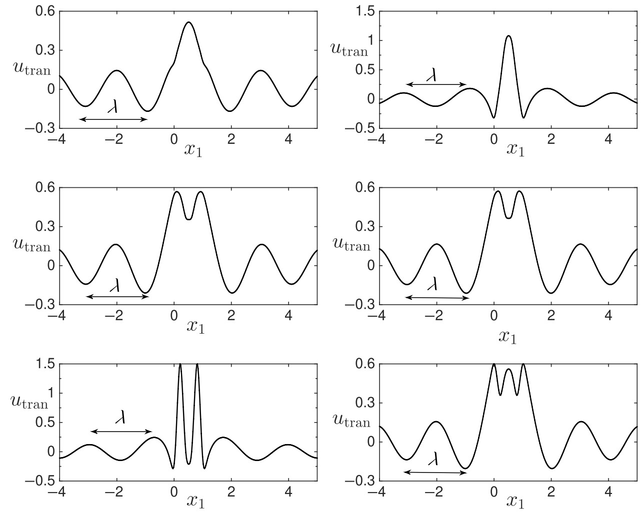

FIG. 3. Real-part value of the transmitted field u_{tran} on the sample plane $x_2 = 0$ at the resonant frequencies $k = \Re\, k_{1j}$ for $j = 1, 2, \ldots, 6$. Note that the x_1 axis is dimensionless and the slit aperture spans the interval $I_{\text{slit}} = [0, 1]$.

This translates into the wave field in the spatial domain:

$$u_{\text{det}}(x_1, d) = \int_{-\infty}^{\infty} e^{i(\xi x_1 + \rho_0(\xi) d)}\, \hat{u}_{\text{samp}}(\xi, 0)\, d\xi, \tag{5}$$

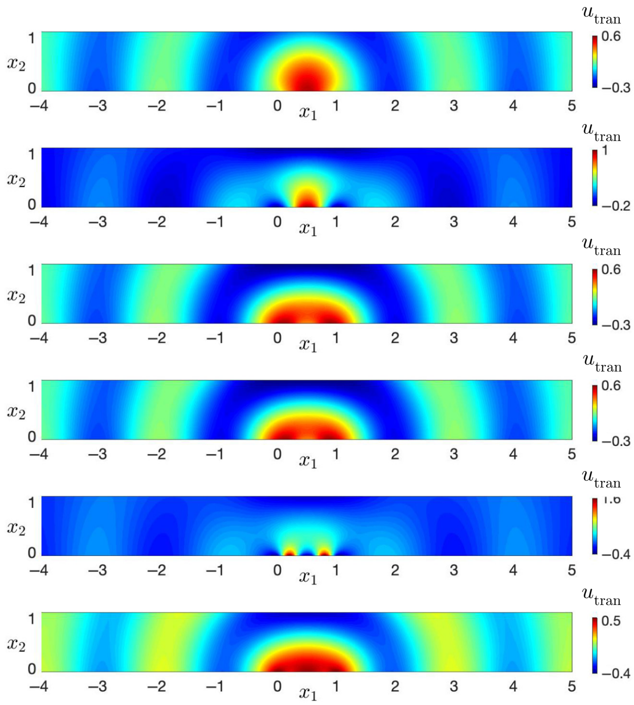

FIG. 4. Real-part value of the transmitted field u_{tran} in the dimensionless region $[-4, 5] \times [0, 1]$ above the sample plane at the resonant frequencies $k = \Re\, k_{1j}$ for $j = 1, 2, \ldots, 6$.

or equivalently, the convolution

$$u_{\mathrm{det}}(\cdot, d) = w_d * u_{\mathrm{samp}} = w_d * (q u_{\mathrm{tran}}), \tag{6}$$

where $\hat{w}_d(\xi) = e^{i\rho_0(\xi)d}$. Due to the exponential decay of the propagator $e^{i\rho_0(\xi)d}$ for large $|\xi|$, in the far field where $d \gg \lambda$, only the plane-wave components with $\xi^2 + \rho_0^2 \leq k^2$ reach the detector plane.

Define $p(x_1) := 1 - q(x_1)$, which vanishes outside the interval I_0. Let I_d be the measurement aperture on the detector plane. We define the operator $A_k : L^2(I_0) \to L^2(I_d)$:

$$A_k[p] = w_d * (p u_{\mathrm{tran}}).$$

Let h_k and $h_k^{(0)}$ be the measurement of the field over the aperture I_d when the sample is present and not, respectively. We seek to recover p by solving the equation

$$A_k[p] + \eta_k = g_k, \tag{7}$$

where $g_k = h_k - h_k^{(0)}$ and η_k denotes the noise. In the case of multiple frequency configuration with incident frequencies $k = k_1, k_2, \ldots, k_m$, we assemble all the data together to solve the equation

$$A[p] + \eta = g, \tag{8}$$

where the operator $A : L^2(I_0) \to \left[L^2(I_d)\right]^m$, the measurement g and the noise η are given by

$$A = \begin{bmatrix} A_{k_1} \\ \cdot \\ \cdot \\ \cdot \\ A_{k_m} \end{bmatrix}, \quad g = \begin{bmatrix} g_{k_1} \\ \cdot \\ \cdot \\ \cdot \\ g_{k_m} \end{bmatrix}, \quad \text{and} \quad \eta = \begin{bmatrix} \eta_{k_1} \\ \cdot \\ \cdot \\ \cdot \\ \eta_{k_m} \end{bmatrix}.$$

B. Reconstruction algorithms

In this section, we apply two numerical algorithms to solve Eq. (8) and reconstruct the function p. One is the gradient-descent regularization method, which yields smooth reconstruction profiles. The other is the total variation regularization, which allows for rougher reconstruction profiles and can capture the sharp edges in the image. An efficient split Bregman iteration is employed to solve the corresponding minimization problem. Both algorithms are computationally inexpensive due to their low complexity for the linear problem (8). A comparison of reconstructed images for the two approaches is given in Sec. III C.

1. Gradient-descent method

To apply the gradient-descent algorithm, one reformulates Eq. (8) as the minimization problem

$$\min_{p \in L^2(I_0)} \|A[p] - g\|_{L^2(I_d)}. \tag{9}$$

Starting from $p_0 = 0$, the iteration is computed as follows:

$$p_{n+1} = p_n + \alpha_n r_n, \quad n \geq 0$$

in which

$$r_n = \Re(A^* g - A^* A p_n), \quad \alpha_n = \frac{\langle r_n, r_n \rangle}{\langle A^* A r_n, r_n \rangle}.$$

In view of Eq. (4), when $d \gg \lambda$ the convolution operator in Eq. (6) is smoothing, which essentially filters the frequency components of a function outside the frequency band Ω_k. Therefore, with the application of the operator A^* at each step, the gradient-descent iteration is very insensitive to the highly oscillatory noise in the measurement. On the other hand, as pointed out in formula (1), the high-spatial-frequency components of the function p outside the band Ω_k is transferred to Ω_k when transmitted wave fields with different oscillation patterns interact with the sample, and these frequency components can be reconstructed from the measurement g. These two features together yield a superresolution imaging of p in a stable manner.

2. Total variation regularization and the split Bregman iteration

To capture the sharp edges in the image, one can apply the total variation regularization for the reconstruction [44]. This boils down to solving the minimization problem

$$\min_p \|p\|_{\mathrm{TV}} + \frac{\alpha}{2} \|A[p] - g\|_{L^2(I_d)}, \tag{10}$$

in which $\alpha > 0$ is the relaxation parameter, and the total variation norm is defined as $\|p\|_{\mathrm{TV}} = \int_{I_0} |p'| dx_1$. The minimization problem (10) is reformulated equivalently as the following constrained optimization problem:

$$\min_p \|s\|_{L^1(I_0)} + \frac{\alpha}{2} \|A[p] - g\|_{L^2(I_d)} \quad s.t.\ s = p', \tag{11}$$

which can be converted to an unconstrained optimization problem with the relaxation parameter $\beta > 0$:

$$\min_{p,s} \|s\|_{L^1(I_0)} + \frac{\alpha}{2} \|A[p] - g\|_{L^2(I_d)} + \frac{\beta}{2} \|s - p'\|_{L^2(I_0)}. \tag{12}$$

The optimization problem (12) can be solved by the Bregman iteration method [45,46]:

$$(p_{n+1}, s_{n+1}) = \text{argmin}_{p,s} \|s\|_{L^1(I_0)} + \frac{\alpha}{2}\|A[p] - g\|_{L^2(I_d)} + \frac{\beta}{2}\|s - p' - b_n\|_{L^2(I_0)},$$

$$b_{n+1} = b_n + s_{n+1} - p'_{n+1}.$$

Here b is an auxiliary variable.

The split Bregman iteration is to split the objective functional into two components and solve for p_{n+1} and s_{n+1} above in an alternative manner [45]. The algorithm is described as follows:

```
: Set $p_0 = 0$, $s_0 = 0$, $b_0 = 0$.
: While $\|p_{n+1} - p_n\|_{L^2(I_0)} > tol$
    : $p_{n+1} = \text{argmin}_p (\alpha/2)\|A[p] - g\|_{L^2(I_d)} + \beta/2\|s_n - p' - b_n\|_{L^2(I_0)}$,
    : $s_{n+1} = \text{argmin}_s \|s\|_{L^1(I_0)} + \beta/2\|s - p'_{n+1} - b_n\|_{L^2(I_0)}$,
    : $b_{n+1} = b_n + s_{n+1} - p'_{n+1}$,
: End
```

Since p and s are decoupled in each subproblem, the optimization for p and s at each iteration can be obtained efficiently by solving a Possion equation for the former and applying a shrinkage operator for the latter [45].

C. Numerical examples

A total of nine slit holes, each with width $\delta = 0.02$, are patterned in a metallic slab of thickness $L = 1$. The distance between two adjacent slit holes is $\ell = 0.5$ and the nine slit apertures span the interval $I_{\text{slit}} := [0, 4]$. Among the nine resonant frequencies $\{k_{1,j}\}_{j=1}^{9}$ near π, we choose six frequencies to generate illumination patterns with distinct features. For each frequency $k_{1,j}$, two illuminations are generated using the real and imaginary part of normal incident wave $e^{ik_{1,j}x_2}$, respectively. The smallest resonant frequency is $k_1 = 2.8301$ and the largest resonant frequency is $k_6 = 2.9695$. In the following examples, we use the wavelength corresponding to the largest resonant frequency (or the shortest wavelength) among 12 illuminations in the discussion of resolution, and this corresponds to a wavelength $\lambda \approx 2$.

We first consider an infinitely thin sample with the transmission function given by $q = 1 - p$, where

$$p = 0.5\chi_{(0.8,1.2)} + 0.8\chi_{(0.8+w,1.2+w)} + 0.6\chi_{(2.5,2.9)} + 0.4\chi_{(2.5+w,2.9+w)}. \quad (13)$$

In the above, χ_I denotes the characteristic function that vanishes outside the interval I. We reconstruct the function over the interval $I_0 = I_{\text{slit}}$, by setting the measurement aperture to be $I_d = [-2\lambda, 4\lambda]$ over the detector plane $x_2 = 5\lambda$. Here and henceforth, 5% Gaussian random noise η_k is added to each set of synthetic data. Figure 5 demonstrates the reconstructions when $w = \lambda/5$ and $w = \lambda/10$, respectively. We observe that both the gradient-descent algorithm and the split Bregman iteration with TV regularization give rise to images with a resolution of $\lambda/10 < \ell/2$.

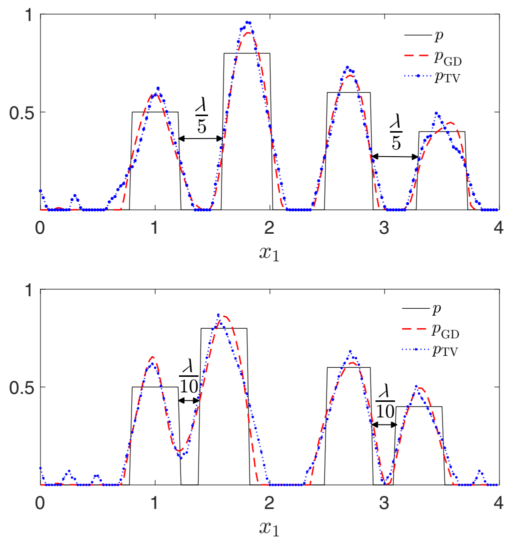

FIG. 5. Reconstruction with the gradient-descent method (p_{GD}) and the TV regularization (p_{TV}) when the dimensionless p is given by (13). Top: $w = \lambda/5$; bottom: $w = \lambda/10$.

In the second example, we use the same subwavelength structure as above and consider the imaging of a multiscale profile, where two small inhomogeneities are embedded in a smooth background. The transmission function is expressed by $q = 1 - p$, in which

$$p = 0.2\left[1 - \cos\left(\frac{\pi}{2}x_1\right)\right]\left[\chi_{I_0} - \chi_{(0.6,1)} - \chi_{(0.6+w,1+w)}\right] + 0.7\chi_{(0.6,1)} + 0.9\chi_{(0.6+w,1+w)}. \quad (14)$$

It is seen from Fig. 6 that both the inhomogeneities and the background are successfully reconstructed, and the image resolution remains the same as in the previous example.

In the third example, we decrease the distance between the slit holes by setting $\ell = 0.25$ so that the slit apertures span the region $I_{\text{slit}} := [0, 2]$. Among the six chosen resonant frequencies, the smallest frequency is $k_1 = 2.7877$ and the largest frequency is $k_6 = 2.9908$. The latter corresponds to a wavelength $\lambda \approx 2$.

Let us consider an infinitely thin sample where

$$p = 0.5\chi_{(0.8-0.5w,1-0.5w)} + 0.8\chi_{(1+0.5w,1.2+0.5w)} + 0.6\chi_{(1.2+1.5w,1.4+1.5w)}. \quad (15)$$

The reconstructions are performed over the interval $I_0 = I_{\text{slit}}$, using the measurement aperture $I_d = [-2\lambda, 3\lambda]$ over the detector plane $x_2 = 5\lambda$. The images obtained from

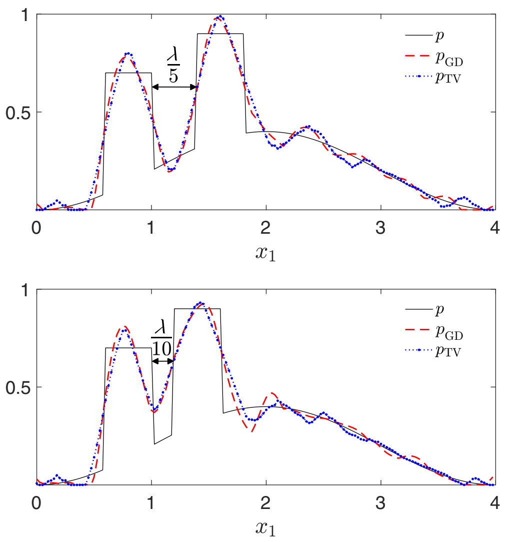

FIG. 6. Reconstruction with the gradient-descent method ($p_{\rm GD}$) and the TV regularization ($p_{\rm TV}$) when the dimensionless p is given by Eq. (14). Top, $w = \lambda/5$; bottom, $w = \lambda/10$.

the two approaches in Fig. 7 show that a resolution of $\lambda/16 \approx \ell/2$ can be achieved. We also observe that in this configuration, the image obtained by the TV regularization has sharper resolution than the one obtained by the gradient-descent algorithm. It should be pointed out that one needs to adjust the relaxation parameters α and β in the TV optimization problem (12) carefully to gain a sharper resolution. The optimal choice of parameters is a delicate and interesting question, and may deserve further investigation.

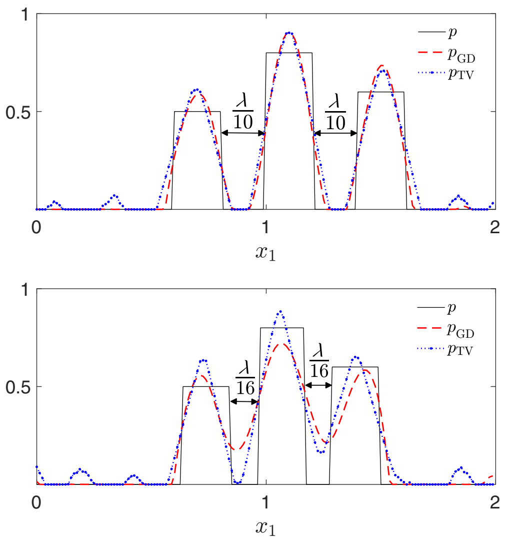

FIG. 7. Reconstruction with the gradient-descent method ($p_{\rm GD}$) and the TV regularization ($p_{\rm TV}$) when the dimensionless p is given by Eq. (15). Top, $w = \lambda/10$; bottom, $w = \lambda/16$.

IV. SUPERRESOLUTION IMAGING OF THIN SAMPLES WITH FINITE THICKNESS

In this section, we consider the configuration where a sample of finite thickness occupies the domain $R_0 \subset D^{(3)}$ above the sample plane. The linear imaging problem is investigated by assuming that the sample is a weak scatterer and using the Born approximation. Let $u_{\rm tran}$ be the transmitted field through the slit holes at the absence of the imaging sample, then the Helmholtz equation for the diffracted field satisfies

$$\Delta u_{\rm diff} + k^2 u_{\rm diff} = -k^2 p\, u_{\rm tran} \quad \text{in } D^{(3)},$$

where $p(x) = \varepsilon(x) - 1$ and the permittivity value $\varepsilon(x) = 1$ outside the region R_0. Using the layered Green function $g^{(3)}(x,y)$ in the domain $D^{(2)} \cup D^{(3)}$ with the Neumann boundary condition along the metallic slab boundary (see the Appendix), the diffracted field in $D^{(3)}$ can be expressed as

$$\begin{aligned} u_{\rm diff}(x) &= -k^2 \int_{R_0} g^{(3)}(x,y) u_{\rm tran}(y)\, p(y) dy \\ &\quad + \sum_{j=1}^{J} \int_{\Gamma_j^{(2)}} g^{(3)}(x,y)(y)\, \partial_{y_2} u_{\rm diff}(y) ds_y \\ &\approx -k^2 \int_{R_0} g^{(3)}(x,y) u_{\rm tran}(y)\, p(y) dy, \end{aligned}$$

where we neglect the field arising from the induced current over the slit apertures $\Gamma_j^{(2)}$ by noting that $\delta \ll 1$.

With the abuse of notations, we still denote forward operator from the imaging sample p to the diffracted field

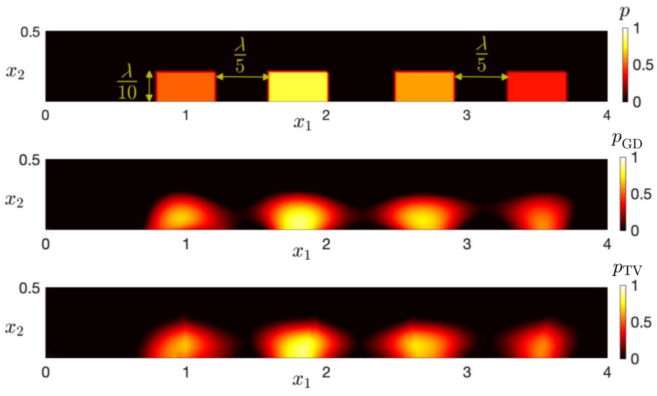

FIG. 8. Real image in the dimensionless domain $R_0 = [0,4] \times [0,0.5]$ (top), and reconstructions with the gradient-descent method (middle), and the TV regularization (bottom). The measurement aperture is $[-2\lambda, 4\lambda]$. The color scale denotes the value of the function $p(x) := \varepsilon(x) - 1$, which is a dimensionless quantity. The same color scale also applies to Figs. 9–14.

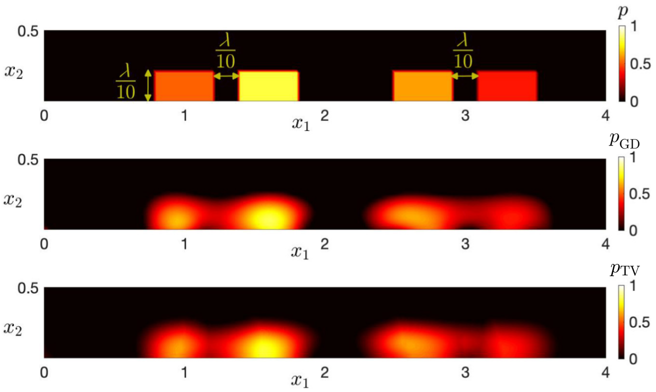

FIG. 9. Real image in the domain $R_0 = [0,4] \times [0,0.5]$ (top), and reconstructions with the gradient-descent method (middle) and the TV regularization (bottom). The same numerical setup as in Fig. 8 is used.

on the detector plane by A_k, which is given by

$$A_k[p] = -k^2 \int_{R_0} g^{(3)}(x_1, d; y) u_{\mathrm{tran}}(y) \, p(y) \, dy.$$

$g_k := u_{\mathrm{diff}} + \eta_k$ is the measurement over the aperture I_d, in which η_k denotes the noise. The reconstruction is performed in the region R_0 by applying both the gradient-descent algorithm and the total variation regularization as discussed in Sec. III. Note that the total variation norm in Eqs. (10)–(12) is now defined as $\|p\|_{\mathrm{TV}} = \int_{R_0} |\nabla p| dx$, and the derivative in the split Bregman iteration is replaced by the gradient ∇. We use the same subwavelength structures as in Sec. III to generate of 12 illumination patterns and the numerical results are discussed below. All the images are plotted in the dimensionless region.

When the distance between the adjacent slit holes is $\ell = 0.5$ and the nine slit apertures span the interval $[0,4]$, we set the reconstruction domain as $R_0 = [0,4] \times [0,0.5]$ and the detector plane is placed over $x_2 = 5\lambda$, where λ again denotes the wavelength corresponding to the largest resonant frequency. Figures 8 and 9 show the real image and the reconstructions when the sample consists of four rectangular shape scatterers. The measurement aperture is $I_d = [-2\lambda, 4\lambda]$ so that the aperture size is 5λ. It is seen that a resolution of $\lambda/10 < \ell/2$ is achieved in both numerical reconstructions. The same subwavelength structure is used to illuminate the sample that consists of two oval-type scatterers embedded in an inhomogeneous background medium, and a resolution $\lambda/5$ is obtained (see Fig. 10). The image quality deteriorates in this scenario as the two scatterers get closer. This is shown in Fig. 11, where the distance between two oval scatterers is $\lambda/10$ for the real image. The loss of accuracy is due to scattering induced by the inhomogeneous background medium.

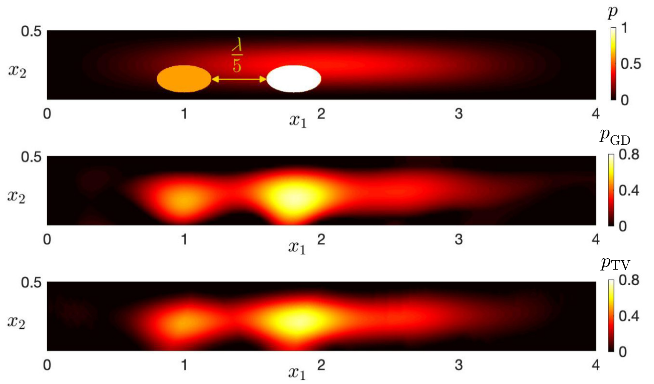

FIG. 10. Real image in the domain $R_0 = [0,4] \times [0,0.5]$ (top), and reconstructions with the gradient descent method (middle) and the TV regularization (bottom). The measurement aperture is $[-2\lambda, 4\lambda]$.

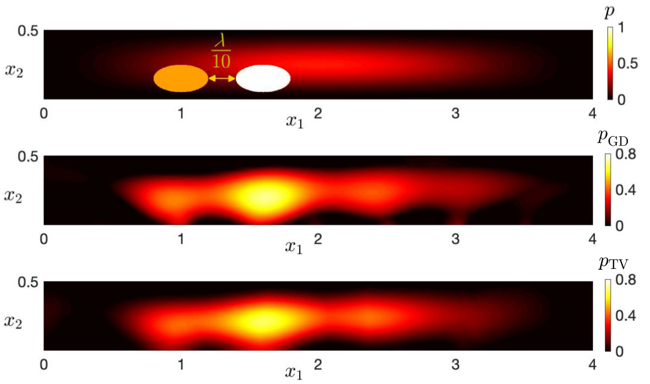

FIG. 11. Real image in the domain $R_0 = [0,4] \times [0,0.5]$ (top), and reconstructions with the gradient-descent method (middle) and the TV regularization (bottom). The same numerical setup as in Fig. 10 is used.

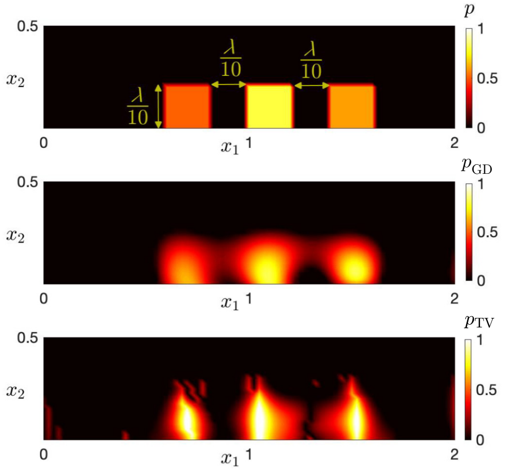

FIG. 12. Real image in the domain $R_0 = [0,2] \times [0,0.5]$ (top), and reconstructions with the gradient-descent method (middle) and the TV regularization (bottom). The measurement aperture is $[-2\lambda, 3\lambda]$.

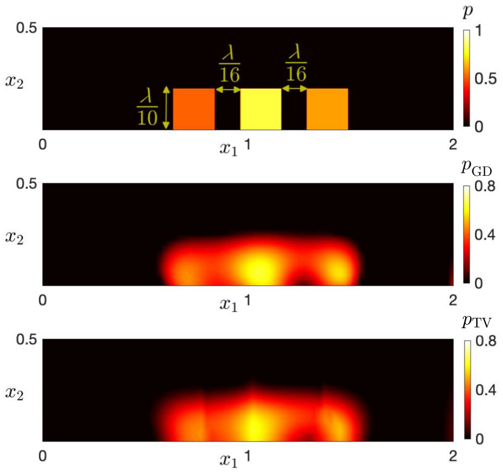

FIG. 13. Real image in the domain $R_0 = [0, 2] \times [0, 0.5]$ (top), and reconstructions with the gradient-descent method (middle) and the TV regularization (bottom). The measurement aperture is $[-2\lambda, 3\lambda]$.

We next decrease the distance between the slit holes to $\ell = 0.25$ so that the slit apertures span the interval $[0, 2]$. The reconstruction is performed in the domain $R_0 = [0, 2] \times [0, 0.5]$. Figures 12 and 13 depict the reconstructed images with a resolution of $\lambda/10$ and $\lambda/16$ ($\approx \ell/2$) respectively, where the measurement aperture is also set as $I_d = [-2\lambda, 3\lambda]$ in the numerical simulation. If one increases the measurement aperture size, then the boundary between the two close scatterers becomes clearer. This is demonstrated in Fig. 14, where the sample in Fig. 13 is reconstructed using the measurement over a larger interval $[-4\lambda, 5\lambda]$. We also point out that, in all numerical examples, the images obtained by the TV regularization attain sharper edges compared with the gradient-descent algorithm.

V. DISCUSSION AND CONCLUSION

In this paper, we present a superresolution imaging approach by using subwavelength hole resonances. An array of resonant holes are arranged close to each other to generate illumination patterns that can probe both the low- and the high-spatial-frequency components of the imaging sample so as to break the diffraction limit. Numerical approaches based on the gradient descent and total variation regularizations are developed to perform the reconstruction from the far-field measurement. It is shown that the resolution of the reconstructed images is determined by the distance between the subwavelength holes. Furthermore, the numerical reconstruction is stable against noise.

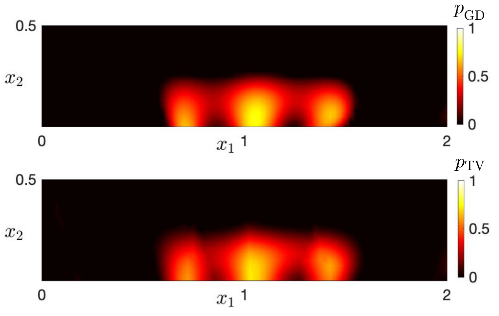

FIG. 14. Reconstructions of the sample in Fig. 13 with the measurement aperture $[-4\lambda, 5\lambda]$. Top, the gradient-descent method; bottom, TV regularization.

In the proposed imaging modality, the sample is deposited on top of the thin substrate and it does not require controlling the distance between the probe and the sample surface with high precision as in near-field microscopies. In addition, compared to the previous imaging approaches using structured illumination, the resolution of the imaging technique is much higher. The experimental investigation of the imaging setup is underway and will be reported elsewhere.

The imaging for the three-dimensional problem is more challenging. In the ongoing studies we use annular subwavelength holes to generate the desired illumination patterns to probe the sample. Another interesting question is to investigate the fully nonlinear inverse problem when multiple scattering between the illumination wave and the imaging sample is significant and the Born approximation fails.

Finally, we point out that the proposed imaging approach allows for a very high lateral resolution in the sample plane. But it can not improve the axial resolution. This is because the highly oscillatory transmitted fields through the subwavelength structures are localized near the slit holes due to their evanescent nature (see Fig. 4), and they can not propagate very deep to probe the sample in the axial direction. The improvement of the resolution in the axial direction is a very challenging problem and deserves further research efforts.

ACKNOWLEDGMENT

The work of J.L. is supported in part by the NSF Grants No. DMS-1719851 and No. DMS-2011148, and the work of H.Z. is supported in part by Hong Kong RGC Grants No. GRF 16305419 and No. GRF 16306318.

APPENDIX A: GREEN’S FUNCTIONS IN THE LAYERED MEDIUM

We derive Green’s function in the layered medium $D^{(2)} \cup D^{(3)}$ with the Neumann boundary condition on the bottom of $D^{(2)}$. Recall that $D^{(2)}$ and $D^{(3)}$ denotes the substrate domain and the domain above the substrate, respectively (see Fig. 2). Green’s function $g^{(3)}(x, y)$ for $y \in D^{(3)}$

satisfies

$$\begin{aligned}
&\Delta_x g^{(3)}(x,y) + k^2\varepsilon(x) g^{(3)}(x,y) = \delta_y \quad \text{in } D^{(2)} \cup D^{(3)},\\
&[g^{(3)}(x,y)] = \left[\frac{1}{\varepsilon}\partial_2 g^{(3)}(x,y)\right] = 0 \quad \text{for } x_2 = 0,\\
&\partial_2 g^{(3)}(x,y) = 0 \quad \text{for } x_2 = -h.
\end{aligned}$$

By taking the Fourier transform of the above equation with respect to the variable $x_1 - y_1$, Green's function in the Fourier domain solves

$$\begin{aligned}
&\widehat{g^{(3)}}''(\xi;x_2,y_2) + (k^2\varepsilon - \xi^2)\widehat{g^{(3)}}(\xi;x_2,y_2) = \delta_{y_2}, \quad x_2 > -h,\\
&[\widehat{g^{(3)}}(\xi;0,y_2)] = \left[\frac{1}{\varepsilon}\widehat{g^{(3)}}'(\xi;0,y_2)\right] = 0,\\
&\widehat{g^{(3)}}'(\xi;-h,y_2) = 0.
\end{aligned}$$

Define

$$\begin{aligned}
&\rho_0(\xi) = \sqrt{k^2\varepsilon_0 - \xi^2}, \quad \rho_h(\xi) = \sqrt{k^2\varepsilon_h - \xi^2},\\
&w_+(\xi) = \rho_0\varepsilon_h(e^{i2\rho_h h} + 1) + \rho_h\varepsilon_0(e^{i2\rho_h h} - 1),\\
&w_-(\xi) = \rho_0\varepsilon_h(e^{i2\rho_h h} + 1) - \rho_h\varepsilon_0(e^{i2\rho_h h} - 1).
\end{aligned}$$

Then the solution of the above equation is given by

$$\widehat{g^{(3)}} = \begin{cases} \dfrac{1}{2i\rho_0} e^{i\rho_0|x_2-y_2|} + R\, e^{i\rho_0(x_2+y_2)} & x_2 > 0,\\ T\cos[\rho_h(x_2+h)]e^{i\rho_0 y_2} & -h < x_2 < 0,\end{cases}$$

where the coefficients

$$R = \frac{w_+}{2i\rho_0 w_-}, \quad T = \frac{2\varepsilon_h e^{i\rho_h h}}{iw_-}.$$

If one decomposes the coefficient R as $R := R_0 + R_1$, in which $R_0 = (1/2i\rho_0)\cdot(\varepsilon_h - \varepsilon_0/\varepsilon_h + \varepsilon_0)$, then $R_1 = O(1/|\xi|^3)$ as $|\xi| \to \infty$. On the other hand, there holds $T = O(e^{-|\xi|h}/|\xi|)$ as $|\xi| \to \infty$.

Let $H_0^{(1)}$ be the first type Hankel function of zero order. By applying the inverse Fourier transform for $\widehat{g^{(3)}}(\xi;x_2,y_2)$ and using the identity

$$\begin{aligned}
&\frac{1}{2\pi}\int_{-\infty}^{\infty} \frac{1}{2i\rho_0(\xi)} e^{i\rho_0(\xi)|x_2-y_2|} e^{i\xi(x_1-y_1)} d\xi\\
&\quad = -\frac{i}{4} H_0^{(1)}(k|x-y|),
\end{aligned}$$

we obtain

$$g^{(3)}(x,y) = \begin{cases} -\dfrac{i}{4}\left[H_0^{(1)}(k|x-y|) + \dfrac{\varepsilon_h - \varepsilon_0}{\varepsilon_h + \varepsilon_0} H_0^{(1)}(k|x'-y|)\right] \\ +g_R^{(3)}(x,y), \quad x \in D^{(3)},\\ g_T^{(3)}(x,y), \quad x \in D^{(2)},\end{cases}$$

where x' is the reflection of x by the x_1 axis. The functions $g_R^{(3)}(x,y)$ and $g_T^{(3)}(x,y)$ are the Sommerfeld integrals given by

$$\begin{aligned}
g_R^{(3)}(x,y) &= \frac{1}{2\pi}\int_{-\infty}^{\infty} R_1 e^{i\rho_0(x_2+y_2)} e^{i\xi(x_1-y_1)} d\xi\\
g_T^{(3)}(x,y) &= \frac{1}{2\pi}\int_{-\infty}^{\infty} T\cos[\rho_h(x_2+h)] e^{i\rho_0 y_2} e^{i\xi(x_1-y_1)} d\xi.
\end{aligned}$$

Following similar calculations as above, it can be shown that Green's function $g^{(2)}(x,y)$ for $y \in D^{(2)}$ takes the following form:

$$g^{(2)}(x,y) = \begin{cases} g_T^{(2)}(x,y), \quad x \in D^{(3)},\\ -\dfrac{i}{4}\left[H_0^{(1)}(kn_h|x-y|) + H_0^{(1)}(kn_h|x'-y|)\right] \\ +g_R^{(2)}(x,y), \quad x \in D^{(2)}.\end{cases}$$

In the above, x' denotes the reflection of x by the line $x_2 = -h$. The corresponding Sommerfeld integrals are

$$\begin{aligned}
g_R^{(2)}(x,y) &= \frac{1}{2\pi}\int_{-\infty}^{\infty} \tilde{R}\Big\{\cos[\rho_h(x_2-y_2)]\\
&\qquad + \cos[\rho_h(x_2+y_2+2h)]\Big\} e^{i\xi(x_1-y_1)} d\xi,\\
g_T^{(2)}(x,y) &= \frac{1}{2\pi}\int_{-\infty}^{\infty} \tilde{T}\cos[\rho_h(y_2+h)] e^{i\rho_0 x_2} e^{i\xi(x_1-y_1)} d\xi,
\end{aligned}$$

where

$$\tilde{R} = \frac{(\rho_h\varepsilon_0 - \rho_0\varepsilon_h)e^{i2\rho_h h}}{i\rho_0\tilde{w}}, \quad \tilde{T} = \frac{2e^{i\rho_h h}}{i\tilde{w}}$$

and

$$\tilde{w} = (\rho_h\varepsilon_0 + \rho_0\varepsilon_h) - (\rho_h\varepsilon_0 - \rho_0\varepsilon_h)e^{i2\rho_h h}.$$

[1] E. Abbe, Beiträge zur theorie des mikroskops und der mikroskopischen wahrnehmung, Archiv Mikroskopische Anatomie **9**, 413 (1873).

[2] L. Novotny and B. Hecht, *Principles of Nano-Optics* (Cambridge University Press, Cambridge, 2006).

[3] L. Rayleigh, On the theory of optical images with special reference to the optical microscope, Phil. Mag. **5**, 167 (1896).

[4] D. Courjon and C. Bainier, Near field microscopy and near field optics, Rep. Prog. Phys. **57**, 989 (1994).

[5] D. Courjon, K. Sarayeddine, and M. Spajer, Scanning tunneling optical microsocpy, Opt. Commun. **71**, 23 (1989).

[6] R. Dunn, Near-field scanning optical microscopy, Chem. Rev. **99**, 2891 (1999).

[7] R. C. Reddick, R. J. Warmack, D. W. Chilcott, S. L. Sharp, and T. L. Ferrell, Photon scanning tunneling microscopy, Rev. Sci. Instrum. **61**, 3669 (1990).

[8] E. Betzig, G. H. Patterson, R. Sougrat, O. W. Lindwasser, S. Olenych, J. S. Bonifacino, M. W. Davidson, J. Lippincott-Schwartz, and H. F. Hess, Imaging intracellular fluorescent proteins at nanometer resolution, Science **313**, 1642 (2006).

[9] S. Hess, T. Girirajan, and M. Mason, Ultra-high resolution imaging by fluorescence photoactivation localization microscopy, Biophys. J. **91**, 4258 (2006).

[10] M. Rust, M. Bates, and X. Zhuang, Stochastic optical reconstruction microscopy (storm) provides sub-diffraction-limit image resolution, Nat. Methods **3**, 793 (2006).

[11] M. Gustafsson, Surpassing the lateral resolution limit by a factor of two using structured illumination microscopy, J. Microsc. **198**, 82 (2000).

[12] M. Gustafsson, Nonlinear structured-illumination microscopy: Wide-field fluorescence imaging with theoretically unlimited resolution, Proc. Nat. Acad. Sci. **102**, 13081 (2005).

[13] S. Hell and J. Wichmann, Breaking the diffraction resolution limit by stimulated emission: Stimulated-emission-depletion fluorescence microscopy, Opt. Lett. **19**, 780 (1994).

[14] G. Bao and P. Li, Near-field imaging of infinite rough surfaces, SIAM J. Appl. Math. **73**, 2162 (2013).

[15] G. Bao and P. Li, Near-field imaging of infinite rough surfaces in dielectric media, SIAM J. Imag. Sci. **7**, 867 (2014).

[16] G. Bao and J. Lin, Near-field imaging of the surface displacement on an infinite ground plane, Inverse Probl. Imag. **2**, 377 (2013).

[17] G. Bao and J. Lin, Imaging of reflective surfaces by near-field optics, Opt. Lett. **37**, 5027 (2012).

[18] P. C. andd, M.Vadim and J. Schotland, Near-field tomography without phase retrieval, Phy. Rev. Lett. **86**, 5874 (2001).

[19] P. Carney and J. Schotland, Inverse scattering for near-field microscopy, Appl. Phys. Lett. **77**, 2798 (2000).

[20] P. Carney and J. Schotland, Three-dimensional total internal reflection microscopy, Opt. Lett. **26**, 2798 (2001).

[21] E. Candès and C. Fernandez-Granda, Towards a mathematical theory of super-resolution, Commun. Pure Appl. Math. **67**, 906 (2014).

[22] D. Donoho, Superresolution via sparsity constraints, SIAM J. Math. Anal. **23**, 1309 (1992).

[23] W. Liao and A. Fannjiang, Music for single-snapshot spectral estimation: Stability and super-resolution, Appl. Comput. Harmon. Anal. **40**, 33 (2016).

[24] P. Liu and H. Zhang, Computational resolution limit: A theory towards super-resolution, (2020).

[25] J. Lin, S. Shipman, and H. Zhang, A mathematical theory for fano resonance in a periodic array of narrow slits, SIAM J. Appl. Math. **80**, 2045 (2020).

[26] J. Lin and H. Zhang, Scattering and field enhancement of a perfect conducting narrow slit, SIAM J. Appl. Math. **77**, 951 (2017).

[27] J. Lin and H. Zhang, Scattering by a periodic array of subwavelength slits I: Field enhancement in the diffraction regime, Multiscale Model. Simul. **16**, 922 (2018).

[28] J. Lin and H. Zhang, Scattering by a periodic array of subwavelength slits II: Surface bound states, total transmission and field enhancement in the homogenization regimes, Multiscale Model. Simul. **16**, 954 (2018).

[29] J. Lin and H. Zhang, An integral equation method for numerical computation of scattering resonances in a narrow metallic slit, J. Comput. Phys. **385**, 75 (2019).

[30] J. Lin and H. Zhang, Mathematical analysis of surface plasmon resonance by a nano-gap in the plasmonic metal, SIAM J. Math. Anal. **51**, 4448 (2019).

[31] J. Lin, S.-H. Oh, and H. Zhang, Sensitivity of resonance frequency in the detection of thin layer using nano-slit structures (to be published).

[32] J. Lin and H. Zhang, Fano resonance in metallic grating via strongly coupled subwavelength resonators, European J. Appl. Math. (to be published).

[33] T. Ebbesen, H. J. Lezec, H. F. Ghaemi, T. T. Thio, and P. A. Wolff, Extraordinary optical transmission through sub-wavelength hole arrays, Nature **391**, 667 (1998).

[34] A. Blanchard-Dionne and M. Meunier, Sensing with periodic nanohole arrays, Adv. Opt. Photonics **9**, 891 (2017).

[35] F. M. Huang, S. K. Tsung, V. A. Fedotov, Y. Chen, and N. I. Zheludev, Nanohole array as a lens, Nano Lett. **8**, 2469 (2008).

[36] S. Oh and H. Altug, Performance metrics and enabling technologies for nanoplasmonic biosensors, Nat. Commun. **9**, 5263 (2018).

[37] S. G. Rodrigo, F. de. Leon-Perez, and L. Martin-Moreno, Extraordinary optical transmission: Fundamentals and applications, Proc. IEEE **104**, 2288 (2016).

[38] F. Lemoult, M. Fink, and G. Lerosey, Acoustic Resonators for Far-Field Control of Sound on a Subwavelength Scale, Phys. Rev. Lett. **107**, 064301 (2011).

[39] H. Ammari and H. Zhang, A mathematical theory of super-resolution by using a system of sub-wavelength helmholtz resonators, Commun. Math. Phys. **337**, 379 (2015).

[40] X. Chen, H.-R. Park, M. Pelton, X. Piao, N. C. Lindquist, H. Im, Y. J. Kim, J. S. Ahn, K. J. Ahn, and N. Park, *et al.* Atomic layer lithography of wafer-scale nanogap arrays for extreme confinement of electromagnetic waves, Nat. Commun. **4**, 1 (2013).

[41] L. Giannuzzi, *Introduction to Focused ion Beams: Instrumentation, Theory, Techniques and Practice* (Springer Science & Business Media, New York, 2004).

[42] H. Ammari, H. Kang, B. Fitzpatrick, M. Ruiz, S. Yu, and H. Zhang, *Mathematical and Computational Methods in Photonics and Phononics*, Mathematical Surveys and Monographs Vol. 235 (American Mathematical Society, Providence, 2018).

[43] Y. Xia and G. Whitesides, Soft lithography, Ann. Rev. Mater. Sci. **28**, 153 (1998).

[44] L. Rudin, S. Osher, and E. Fatemi, Nonlinear total variation based noise removal algorithms, Phys. D: Nonlinear Phenom. **60**, 259 (1992).

[45] T. Goldstein and S. Osher, The split Bregman method for l1-regularized problems, SIAM J. Imaging Sci. **2**, 323 (2009).

[46] S. Osher, M. Burger, D. Goldfarb, J. Xu, and W. Yin, An iterative regularization method for total variation-based image restoration, Multicale Model. Simul. **4**, 460 (2005).